International Journal of Solids and Structures 244-245 (2022) 111563

Contents lists available at ScienceDirect

International Journal of Solids and Structures

journal homepage: www.elsevier.com/locate/ijsolstr

On fracture anisotropy in textured aluminium alloys

Bjørn Håkon Frodal *, Susanne Thomesen, Tore Børvik, Odd Sture Hopperstad

SIMLab – Structural Impact Laboratory, Department of Structural Engineering, NTNU – Norwegian University of Science and Technology, Trondheim, Norway
CASA – Centre for Advanced Structural Analysis, NTNU, Trondheim, Norway

ARTICLE INFO

Keywords:
Ductile fracture
Crystal plasticity
Finite element method
Fracture anisotropy
Aluminium alloys

ABSTRACT

The yielding, plastic flow and fracture of textured aluminium alloys depend on their microstructure formed during the thermo-mechanical processing. In this work, we investigate two extruded aluminium alloys with different yield strength, work hardening, grain structure, crystallographic texture and tensile ductility. To study the fracture anisotropy of these alloys, i.e., the variation in the failure and fracture strain with loading direction, finite element simulations of an axisymmetric smooth tensile specimen are compared to experimental tests in five in-plane directions with respect to the extrusion direction. A newly proposed coupled damage and single crystal plasticity model is used in three-dimensional finite element analyses of the tensile tests. The tensile tests are simulated in Abaqus/Explicit, where each grain is explicitly modelled. This modelling framework is able to capture the effects of the heterogeneous yielding and plastic flow on ductile fracture, caused by the differences in the crystallographic orientation between grains, such as shear bands which may promote strain localization and ductile fracture. The overall agreement between the experimental and numerical results with respect to the plastic anisotropy, i.e., the anisotropy in yielding, plastic flow and work hardening, highlights the important role played by the crystallographic texture. Plastic anisotropy is found to have a marked influence on the tensile ductility and to induce fracture anisotropy. By particularly accounting for the crystallographic texture, the finite element simulations are able to capture the fracture anisotropy observed in the experimental tests.

1. Introduction

During the production of components made of metallic materials, the material goes through a series of thermo-mechanical processing steps. These processing steps are often crucial to produce a material with the desired mechanical properties, but can also introduce effects that are challenging to account for in the engineering and design of structural components. Rolled plates and extruded profiles typically exhibit anisotropic material properties, which increase the complexity of the material modelling. However, the rolling or extrusion process can significantly increase the ductility of a material by breaking up and re-distributing the constituent particles (Tomstad et al., 2021). The thermo-mechanical processing of a material can also influence microstructural features such as the grain structure, crystallographic texture, and precipitate structure (Frodal et al., 2020b) along with the characteristics of the constituent particles. These features of the microstructure determine the properties of a material, such as the yield strength, work hardening, plastic anisotropy, and ductile fracture characteristics, and are thus essential for the plastic response and fracture of metals and alloys.

Ductile fracture involves nucleation, growth and coalescence of microscopic voids at constituent particles. In addition, voids may pre-exist in the material (Campbell, 2011; Toda et al., 2013), and during plastic deformation voids may nucleate around constituent particles either by decohesion or by particle cracking (Maire et al., 2011; Frodal et al., 2017). Further, these voids grow inside the material by plastic straining, and as the inter-void ligaments become subjected to plastic flow localization, the voids coalesce and final rupture of the material is imminent (Pineau et al., 2016). Through this damage process, it is evident that plastic flow and ductile fracture are coupled phenomena. The voids and particles are located inside the grains of the material or at the grain boundaries between different grains. It thus transpires that the local microstructural properties of the grains, their interaction, and local stress state are of utmost importance for ductile fracture in metallic materials (Morgeneyer et al., 2021).

On the macroscopic level, the influence of different microscopic material characteristics can be observed and quantified in experiments such as tensile tests (Chen et al., 2011; Hannard et al., 2018; Madi et al., 2019; Marteleur et al., 2021; Thomesen et al., 2021; Tomstad

* Corresponding author at: SIMLab – Structural Impact Laboratory, Department of Structural Engineering, NTNU – Norwegian University of Science and Technology, Trondheim, Norway.
E-mail address: bjorn.h.frodal@ntnu.no (B.H. Frodal).

https://doi.org/10.1016/j.ijsolstr.2022.111563
Received 14 September 2021; Received in revised form 20 December 2021; Accepted 8 March 2022
Available online 19 March 2022

et al., 2021). For ductile materials, plastic flow governs the majority of the deformation process. As a result, the local stress state is determined by the yielding and plastic flow of the material and influences the ductility measured in experiments (Frodal et al., 2020a). Formed structural components, rolled plates and extruded profiles typically exhibit plastic anisotropy. The strength of the plastic anisotropy varies depending on the thermo-mechanical processing, and is mostly determined by the crystallographic texture of an alloy (Engler and Randle, 2009). If the material exhibits plastic anisotropy, the measured ductility could also depend on the direction of loading and induce fracture anisotropy, i.e., a variation in the failure and fracture strain with loading direction (Chen et al., 2011; Fourmeau et al., 2011, 2013; Morin et al., 2018; Khadyko et al., 2019; Frodal et al., 2020a; Thomesen et al., 2021). In addition, the characteristics of the void nucleating particles in a material, such as their shape, orientation and spatial distribution, can induce fracture anisotropy (Madi et al., 2019), also for materials exhibiting nearly isotropic yielding and plastic flow (Hannard et al., 2018; Marteleur et al., 2021). The damage process may further introduce anisotropy effects by, e.g., favouring particle cracking in certain material directions (Agarwal et al., 2002). Thus, the three main sources of anisotropic fracture in ductile metals are found to be: *plastic anisotropy*, which primarily stems from the crystallographic texture, *morphological anisotropy*, which originates from the shape and preferred orientation of particles and voids, and *topological anisotropy*, which is a result of the spatial distribution of particles and voids (Hannard et al., 2018). Precipitate strengthened aluminium alloys may also exhibit fracture anisotropy due to the precipitate free zones (PFZs) along grain boundaries that may promote strain localization (Steglich et al., 2008).

Based on unit cell analyses, Keralavarma et al. (2011) found that the void aspect ratio, in addition to the plastic anisotropy, can significantly affect the overall ductility of anisotropic materials. Using three-dimensional unit cell simulations, Legarth and Tvergaard (2018) investigated the three main sources of anisotropic fracture. They showed that the presence of plastic anisotropy amplified the effects of the morphological and topological anisotropy, and that there was a clear interaction between the effects of plastic anisotropy, void spacing, and void shape. Plastic anisotropy can also trigger shear bands that may be detrimental for the ductility of a material (Torki and Benzerga, 2018; Benzerga et al., 2019). Morin et al. (2018) and Frodal et al. (2020a) performed strain localization analyses of tensile tests in different material directions of 6000- and 7000-series aluminium alloys with distinct grain structure and crystallographic texture. These investigations showed that the anisotropy in failure correlates with the plastic anisotropy as described by the variation of the Lankford coefficient for these alloys. The observations from the strain localization analyses conform well with experimental tests of aluminium alloys with similar microstructure (Fourmeau et al., 2013; Khadyko et al., 2019; Thomesen et al., 2021).

Plastic anisotropy is usually modelled and included in a constitutive framework by an anisotropic yield criterion (e.g., Hill, 1948; Bron and Besson, 2004; Barlat et al., 2005). These anisotropic yield criteria typically incorporate one or several linear transformations of the stress tensor (Barlat et al., 2005), and are usually calibrated from either a large number of experimental tests (Fourmeau et al., 2011) or crystal plasticity simulations of representative volume elements (RVEs) (Zhang et al., 2015, 2016; Frodal et al., 2019). Based on information about a material's crystallographic texture, crystal plasticity theory can be used to determine its plastic flow properties. The grain morphology as well as the local interactions and inhomogeneities of the mechanical fields of polycrystalline materials can all be explicitly included in crystal plasticity analyses (Frodal et al., 2021). In addition, changes in the plastic properties of a material can be modelled by evolving the texture during deformation (Li et al., 2005; Wu et al., 2007; Kalidindi et al., 2009; Prakash et al., 2009; Lu et al., 2011; Jia et al., 2012; Feather et al., 2019; Ghorbanpour et al., 2020). Due to the computational cost of crystal plasticity models, they are rarely used in three-dimensional finite element simulations of material test specimens or structural components. Ductile fracture adds another layer of complexity and increases the computational cost. Few studies have used crystal plasticity to investigate ductile fracture in anisotropic polycrystalline materials, and the effects of, e.g., crystallographic texture, texture evolution and polycrystalline heterogeneity on ductile fracture are still open questions. In single and oligo-crystal specimens, the crack path, ductility and fracture toughness have been observed to be highly dependent on the crystallographic orientations of grains (Scherer et al., 2021). Using in-situ synchrotron laminography imaging together with crystal plasticity finite element analyses, Morgeneyer et al. (2021) found that the crystallographic effects play an important role in heterogeneous plastic flow and that this heterogeneity was identified as the precursor to final localization and slant fracture. The influence of these microstructural features on the macroscopic behaviour of metals and alloys is not well established and requires further research. Recently, Frodal et al. (2021) proposed an accurate, robust and computationally efficient coupled damage and single crystal plasticity model, and used the model in three-dimensional polycrystalline finite element simulations of engineering test specimens of four aluminium materials. By explicitly modelling each grain, they were able to investigate and describe phenomena that regular plasticity models cannot, such as the influence of the heterogeneous stress and strain fields caused by the discrete nature of the grain morphology during ductile fracture.

In this study, fracture anisotropy in textured aluminium alloys is investigated. The coupled damage and single crystal plasticity model proposed by Frodal et al. (2021) is used in polycrystalline finite element simulations of smooth axisymmetric tensile specimens where each grain is explicitly modelled. Simulations of tensile tests are performed in five in-plane directions, i.e., 0°, 22.5°, 45°, 67.5° and 90° with respect to the extrusion direction. The three-dimensional finite element simulations are compared to experimental tests on two extruded aluminium alloys with different yield strength, work hardening, grain structure, crystallographic texture, and tensile ductility. The overall agreement between the numerical and experimental results indicates the strong influence of crystallographic texture on the plastic anisotropy. The finite element simulations consider the heterogeneous mechanical fields introduced by the microstructure in polycrystalline materials, and are able to account for the local microstructural properties of the grains, their interaction and local stress state, which are important for a realistic description of ductile fracture. As a result, the distinct fracture anisotropy observed experimentally for the two alloys is captured by the coupled damage and single crystal plasticity model by accounting for the crystallographic texture in the finite element analyses.

2. Materials and experimental background

Extruded profiles of the aluminium alloys AA6063 and AA6110 are considered. Experimental data for these alloys have previously been reported in Thomesen (2019) and Thomesen et al. (2021), and the reader is referred there for further details regarding the materials, material characterization and mechanical testing. A brief summary of the experimental background is given below.

Tensile test specimens of the two alloys were machined from the extruded profiles, which had been solution heat-treated and artificially aged to peak strength (temper T6). The AA6063 alloy has a recrystallized grain structure comprising of almost equi-axed grains measuring on average 40 μm along the extrusion direction (ED), 36 μm along the transverse direction (TD), and 30 μm along the thickness direction (ND) of the extruded profile. A typical fibrous, non-recrystallized grain structure is found for the extruded AA6110 alloy, where the grains are severely elongated along the ED and have a thickness of approximately 4 μm along the ND. The measured area fraction of constituent particles for the two materials is approximately 0.006 and 0.008 for the AA6063 and AA6110 alloys, respectively.

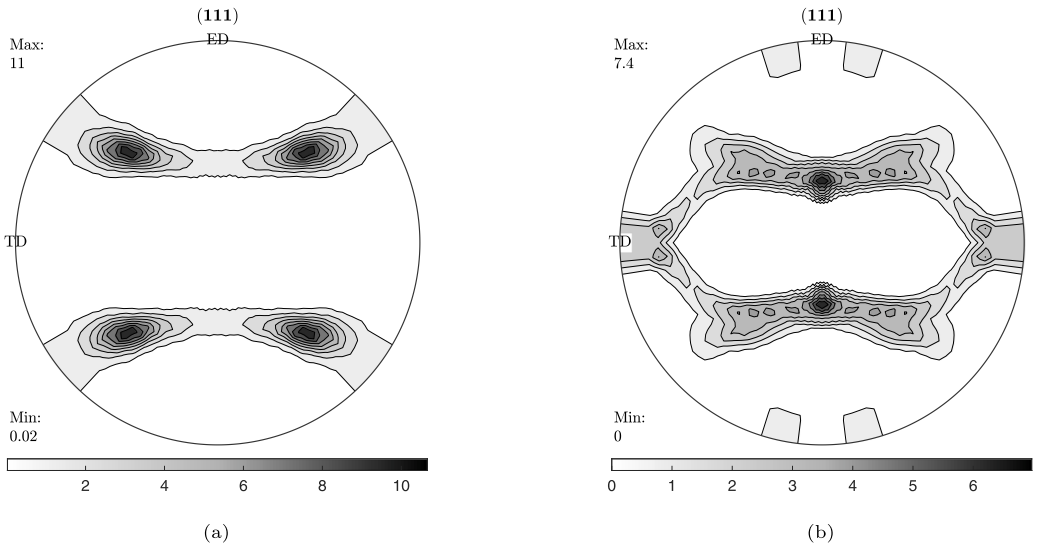

Fig. 1. Pole figures (111) of the initial texture of: (a) the extruded AA6063 alloy, and (b) the extruded AA6110 alloy.

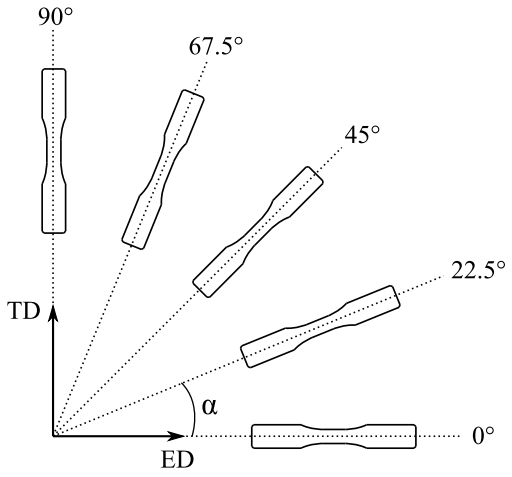

Fig. 2. A schematic drawing of the sample extraction from the extruded profiles as a function of the tensile direction α.

Due to the extrusion process, the alloys exhibit crystallographic texture, see Fig. 1. The AA6063 alloy has a typical recrystallization texture containing a strong cube texture with a minor Goss component. In contrast, the fibrous AA6110 alloy has a classical deformation texture consisting of a cube texture and orientations along the β-fibre.

Tensile tests on smooth axisymmetric specimens were carried out. The specimens were machined from the extruded profiles at different angles α with respect to the ED in the ED–TD plane to characterize the anisotropic material behaviour of the alloys. The ND of the specimen and profile coincided in all cases, while the tensile direction of the specimen made the angle α with the ED of the profile. The test series consisted of repeat tension tests in the 0°, 22.5°, 45°, 67.5° and 90° directions, see Fig. 2, which were carried out at room temperature under displacement control using a universal testing machine. Quasi-static conditions were assured by applying a constant cross-head velocity of 0.15 mm/min, corresponding to an initial strain rate of approximately $\dot{\varepsilon} = 5 \cdot 10^{-4}$ s^{-1}. The geometry of the smooth axisymmetric specimen is shown in Fig. 3.

Continuous measurements of the force and the diameters at the minimum cross section in two perpendicular directions by means of a contact-less laser gauge (Frodal et al., 2017) were provided until fracture. From the diameter measurements, the initial and current areas were calculated as $A_0 = \frac{\pi}{4} D_0^2$ and $A = \frac{\pi}{4} D_{\mathrm{ND}} D_{\perp}$, respectively, where D_0 is the initial specimen diameter, and D_{ND} and $D_{\perp}$ are the measured diameters in the thickness direction and the direction perpendicular to the tensile direction α in the ED–TD plane, respectively. The true stress and logarithmic strain are calculated as

$$\sigma_t = \frac{F}{A}, \quad \varepsilon_l = \ln\left(\frac{A_0}{A}\right) \tag{1}$$

where F is the measured force. The logarithmic strain is calculated under the assumptions of small elastic strains and plastic incompressibility. After necking the stress and strain fields are no longer uniform over the gauge region of the specimen, and the calculated true stress and logarithmic strain represent average values over the minimum cross section of the specimen.

3. Finite element modelling

3.1. Constitutive model

A rate-dependent single crystal plasticity formulation is adopted where plastic deformation is assumed to occur by plastic slip on certain crystallographic slip systems, determined by the crystal structure. The coupled damage and single crystal plasticity model proposed by Frodal et al. (2021) is used in this study. By applying this model, it is assumed that the elastic deformations are infinitesimal, while the plastic deformations and rotations may be finite.

Damage within the crystal plasticity framework is introduced by the use of an effective stress tensor $\tilde{\boldsymbol{\sigma}}$ (Lemaitre, 1985; Frodal et al., 2021), which accounts for the presence of voids or micro-cracks in the single crystal. The effective stress tensor acts on the undamaged portion of the material volume and is defined as

$$\tilde{\sigma}_{ij} = \frac{\sigma_{ij}}{1-\omega} \tag{2}$$

where $\boldsymbol{\sigma}$ is the Cauchy stress tensor and the damage variable $0 \leq \omega \leq \omega_c < 1$ is zero for a completely undamaged material and reaches the critical value ω_c when failure occurs. In the co-rotated coordinate system, see Frodal et al. (2021), the rate form of the generalized Hooke's law can be expressed as

$$\hat{\dot{\tilde{\sigma}}}_{ij} = \hat{\mathbb{C}}_{ijkl} \hat{D}^e_{kl} \tag{3}$$

where the fourth-order elasticity tensor $\mathbb{C}$ of the undamaged portion of the material is assumed invariant of plastic deformation and constant in the co-rotational lattice frame, and $\mathbf{D}^e$ is the elastic part of the rate of deformation tensor. A superimposed hat ($\hat{\blacksquare}$) indicates that the tensor

components refer to the co-rotational coordinate system. The Cauchy stress tensor is found after the stress update by means of Eq. (2). The elasticity tensor accounts for the elastic anisotropy of the crystal and is defined by the three independent elastic constants $\hat{c}_{11}$, $\hat{c}_{12}$ and $\hat{c}_{44}$ in the co-rotated coordinate system.

Plastic flow is described by the following rate-dependent constitutive relation, giving the plastic slip rate on slip system α, as

$$\dot{\gamma}^{(\alpha)} = \dot{\gamma}_0 \left| \frac{\tau^{(\alpha)}}{(1-\omega)\,\tau_c^{(\alpha)}} \right|^{\frac{1}{m}} \operatorname{sgn}\left(\tau^{(\alpha)}\right) \tag{4}$$

where $\dot{\gamma}_0$ is the reference shearing rate, m is the instantaneous strain rate sensitivity, $\tau^{(\alpha)}$ is the resolved shear stress and $\tau_c^{(\alpha)}$ is the critical resolved shear stress on slip system α. The critical resolved shear stresses, with initial value τ_0, evolve according to

$$\dot{\tau}_c^{(\alpha)} = \theta(\Gamma) \sum_{\beta=1}^{N} q_{\alpha\beta} \left| \dot{\gamma}^{(\beta)} \right| \tag{5}$$

where $q_{\alpha\beta}$ is the latent hardening matrix. The work-hardening rate $\theta(\Gamma)$ is given by the extended Voce hardening rule as

$$\theta(\Gamma) = \sum_{k=1}^{N_\tau} \theta_k \exp\left(-\frac{\theta_k}{\tau_k}\Gamma\right) \tag{6}$$

where Γ is the accumulated plastic shear strain, N_τ is the number of hardening terms, and θ_k and τ_k are the initial hardening rate and saturated value of hardening term k, respectively. In the following, $N_\tau = 2$ will be used.

The damage variable, with initial value ω_0, evolves according to (Frodal et al., 2021)

$$\dot{\omega} = \frac{3}{4} q_1 q_2 \omega (1-\omega) \sinh\left(\frac{3}{2} q_2 T\right) \dot{\Gamma} \tag{7}$$

where q_1 and q_2 are material parameters and $\dot{\Gamma}$ is the accumulated plastic shear strain rate. Note that the damage evolution rule (Eq. (7)) is approximately equal to the Rice–Tracey model for moderate and high stress triaxiality ratios (Rice and Tracey, 1969; Rousselier, 1987), and that the evolution of the void volume fraction for the Gurson–Tvergaard model (Gurson, 1977; Tvergaard, 1981) reduces to Eq. (7) for small void volume fractions. The stress triaxiality ratio T is defined as

$$T = \frac{\sigma_h}{\sigma_{vm}} \tag{8}$$

where $\sigma_h = \frac{1}{3}\sigma_{kk}$ is the hydrostatic stress, $\sigma_{vm} = \sqrt{\frac{3}{2}\sigma'_{ij}\sigma'_{ij}}$ is the von Mises equivalent stress, and $\boldsymbol{\sigma}'$ is the deviatoric part of the Cauchy stress tensor.

For a complete description of the coupled damage and single crystal plasticity model, the reader is referred to Frodal et al. (2021).

3.2. Finite element models

In this section, we will introduce the finite element models used to simulate the behaviour of the two extruded aluminium alloys presented in Section 2. The coupled damage and single crystal plasticity model described above is implemented into a user material subroutine (VUMAT) for Abaqus/Explicit. In the following it will be used in finite element simulations of tension tests on smooth axisymmetric tensile specimens in five in-plane material directions and compared to the experimental results.

Fig. 3 displays the geometry and finite element mesh of the smooth tensile specimen. The tensile axis of the specimen will be oriented along five different material directions in the ED–TD plane, i.e., in the 0°, 22.5°, 45°, 67.5°, and 90° direction with respect to the extrusion direction (ED). Due to the orthotropic sample symmetry and the orientations of the specimen, only one-half of the specimen is modelled to reduce the computational time. Linear eight-node elements with selective reduced integration (C3D8) are used, where the dimension of the centre-most elements located within the gauge section of the specimen is $50 \times 50 \times 50$ μm^3. This element size is comparable to but slightly larger than the equi-axed grains of the AA6063 alloy. In contrast, the fibrous grain structure of the AA6110 alloy consist of largely elongated grains, see Section 2.

Table 1
Crystal plasticity parameters governing elasticity, rate sensitivity and latent hardening for the aluminium alloys (Frodal et al., 2019).

$\hat{c}_{11}$ (MPa)	$\hat{c}_{12}$ (MPa)	$\hat{c}_{44}$ (MPa)	$\dot{\gamma}_0$ (s^{-1})	m	$q_{\alpha\beta}$
106 430	60 350	28 210	0.010	0.005	1.0 if $\alpha = \beta$ 1.4 if $\alpha \neq \beta$

In the model, each grain is represented by a single element, and all elements/grains are given initial orientations to account for the crystallographic texture of the two alloys. The crystal orientations are generated using the open source Matlab toolbox MTEX (Bachmann et al., 2010), and the measured texture, i.e., the orientation distribution function (ODF), is used to generate a set of orientations representing the texture for each alloy. In this way, it is ensured that the overall crystallographic texture of the finite element model is the same as the measured texture of the actual alloy.

The specimen is loaded with a nominal strain rate of $\dot{\varepsilon} = 5 \cdot 10^{-4}$ s^{-1} in all simulations, and mass scaling is used to reduce the computational time. Throughout the simulations it is ensured that the response is quasi-static, and it is confirmed that the kinetic energy is negligible.

Table 1 contains the crystal plasticity parameters controlling the elastic behaviour, the rate dependence and the self- and latent hardening, which are common for a broad range of aluminium alloys found in the literature. These parameters are assumed constant for the alloys at hand, while the parameters governing initial slip resistance, work hardening, damage and failure are dependent upon the material processing and alloy composition. The initial damage ω_0 of each alloy is taken equal to the area fraction of constituent particles, see Section 2. The initial slip resistance, work hardening, damage and failure parameters, given in Table 2, have previously been calibrated using smooth and notched tensile specimens pulled along TD, i.e., the 90° direction. Fracture is modelled by element erosion and an element is deleted when $\omega = \omega_c$ in one of the element's integration points. The reader is referred to Frodal et al. (2021) for further details regarding the calibration process.

4. Results

The true stress versus logarithmic strain curves from the crystal plasticity finite element analyses and the experimental tests of the smooth tensile specimen in five material directions are shown in Fig. 4. The overall agreement between the numerical and experimental results indicates the strong influence of the crystallographic texture on the directional stress–strain response. Of particular interest is the ability of the finite element analyses to describe the different hardening slopes at large strains. For the AA6063 alloy it is apparent that the hardening rate at large strains varies markedly between the distinct tensile directions both in the numerical analyses and the experimental tests. In contrast, the hardening rate observed at large strains for the AA6110 alloy is similar in different tensile directions both in the simulations and the experimental tests. These differences in the work-hardening behaviour at large strains are attributed to texture evolution and the fact that the texture may evolve differently in different directions depending on the initial texture of the alloy (Thomesen et al., 2021). From the figure, it is also clear that the point of failure, which is defined here as the point of maximum true stress, varies with tensile direction, and that plastic anisotropy introduced by the crystallographic texture induces fracture anisotropy.

Fig. 5 presents the normalized yield stress versus tensile direction in the ED–TD plane from the crystal plasticity finite element analyses and

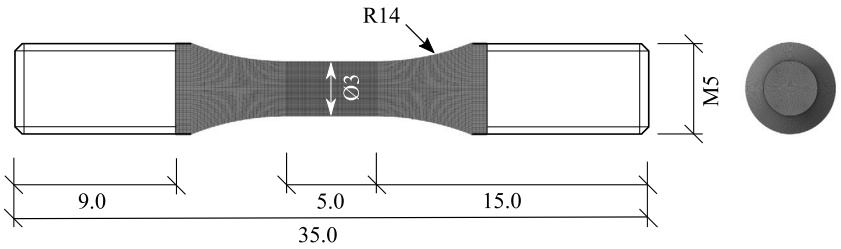

Fig. 3. Smooth axisymmetric tensile specimen used for the two alloys with the finite element mesh superimposed. Dimensions are in mm.

Table 2
Crystal plasticity parameters governing initial slip resistance, work hardening, damage evolution and failure for the aluminium alloys (Frodal et al., 2021).

Alloy	τ_0 (MPa)	θ_1 (MPa)	τ_1 (MPa)	θ_2 (MPa)	τ_2 (MPa)	ω_0	ω_c	q_1	q_2
AA6063	84.7	200.2	20.4	0.0	0.0	0.006	0.12	0.640	1.00
AA6110	96.9	177.4	21.3	3.2	$3.5 \cdot 10^6$	0.008	0.12	0.667	1.10

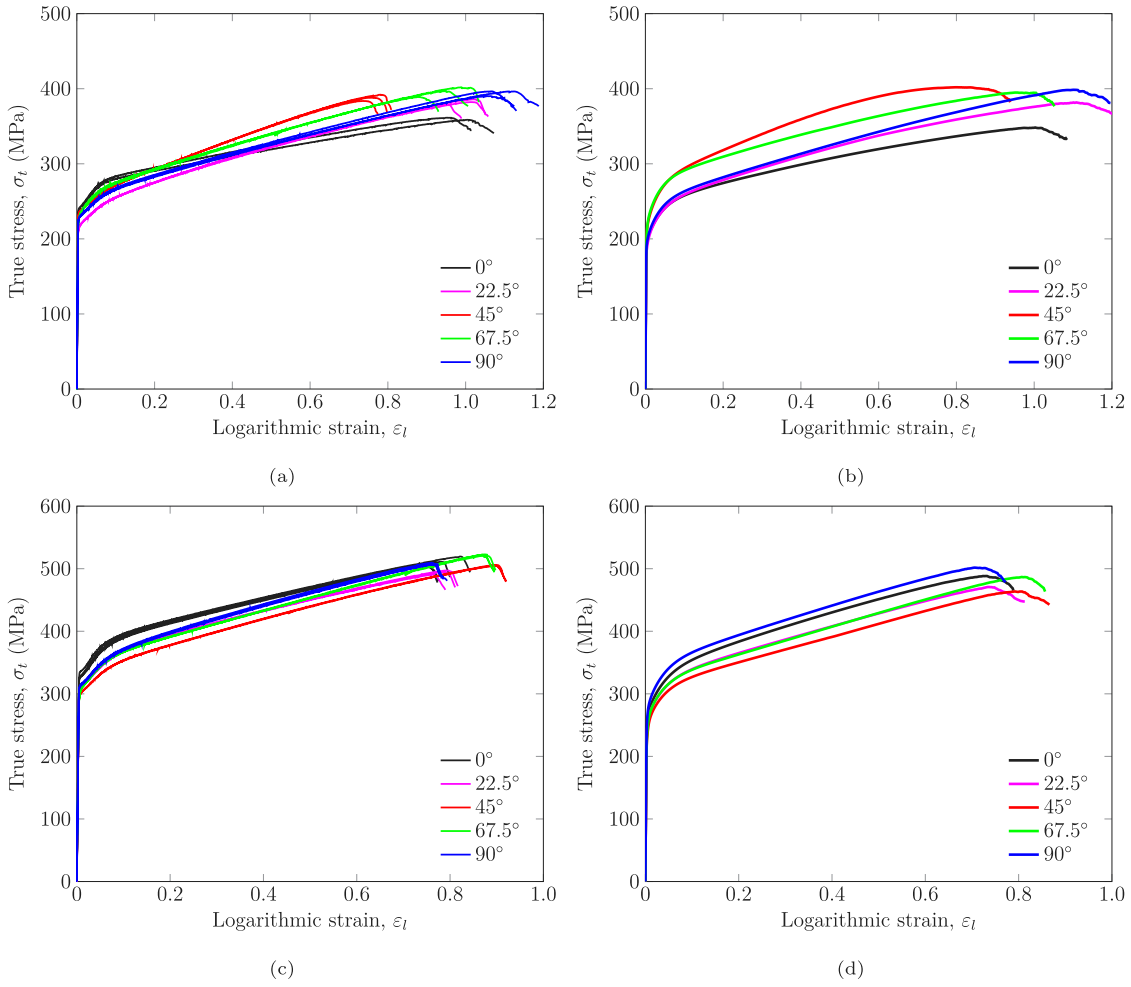

Fig. 4. True stress versus logarithmic strain curves from the experiments and corresponding finite element analyses of the smooth tensile specimens. Experiments (left), simulations (right), AA6063 alloy (top) and AA6110 alloy (bottom).

experimental tests. The normalized yield stress (stress ratio) is defined as

$$r_\alpha = \frac{\sigma_\alpha}{\sigma_0} \tag{9}$$

where σ_α is the yield stress along tensile direction α, and σ_0 is the yield stress along the ED, i.e., the 0° direction. The differences in the yield stress with tensile direction observed in Fig. 4 can be better examined in Fig. 5. Owing to the crystallographic texture that is different for the two alloys, there is a clear difference in the variation of the normalized yield stress with tensile direction for the alloys. The finite element simulations capture the overall experimental trends in the distribution of the normalized yield stress as a function of the tensile direction for both alloys. The two exceptions are the yield stress in the 0° direction for the AA6063 alloy which is too low, and the normalized yield stress in the 90° direction for the AA6110 alloy which is too high in the finite element analyses. However, the overall accuracy in the normalized yield stress is seen to be better for AA6110 than for AA6063. It has

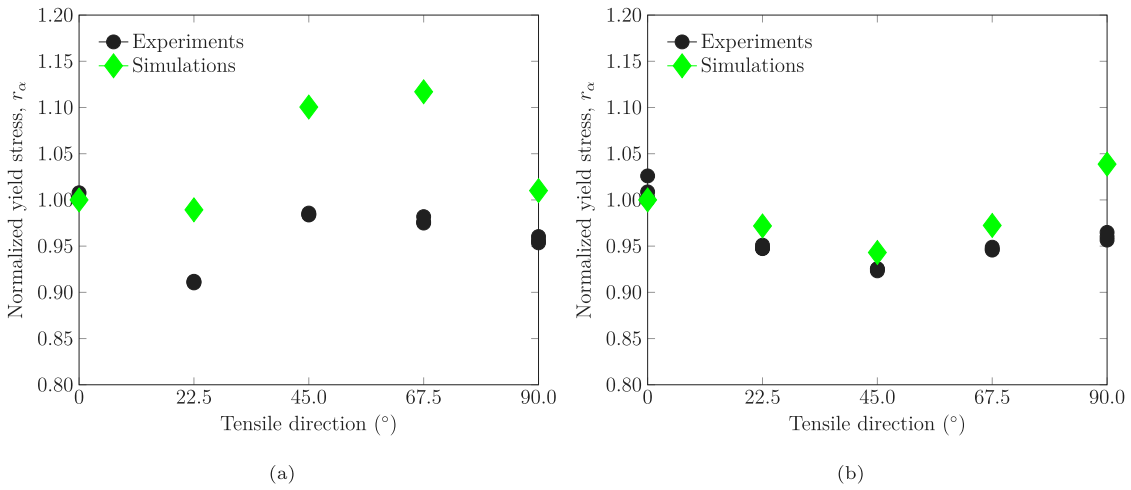

Fig. 5. Normalized yield stress versus tensile direction for the (a) AA6063 alloy and (b) AA6110 alloy at a plastic work corresponding to 0.01 plastic strain.

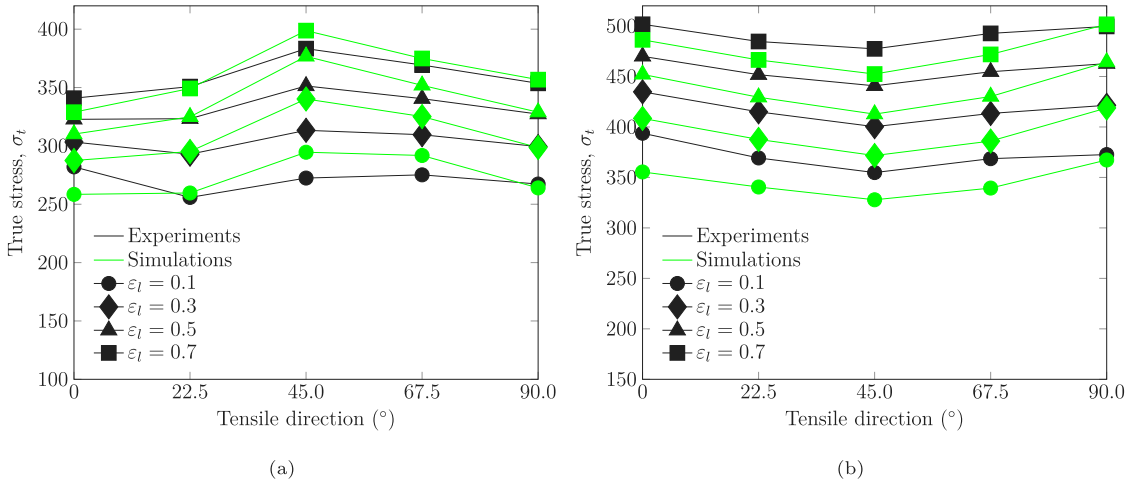

Fig. 6. True stress versus tensile direction for the (a) AA6063 alloy and (b) AA6110 alloy at different levels of logarithmic strain ε_l.

previously been found that the yield stress variation for the AA6063 alloy is dependent on the heat treatment of the alloy (Khadyko et al., 2017), and this is a feature that the work-hardening model used in the present study is unable to describe.

The evolution of the strength anisotropy with plastic straining is further visualized in Fig. 6, where the true stress σ_t at different values of the logarithmic strain ε_l is plotted against the tensile direction α. Fig. 6 shows largely the same trends as observed in Fig. 5. In addition, the strength anisotropy is seen to evolve with plastic straining for the AA6063 alloy, whereas the variation in the true stress with tensile direction is reasonably constant for the AA6110 alloy. A better agreement between the experiments and numerical simulations is observed for the AA6063 alloy at large strains, where the effects of the crystallographic texture dominate the response.

The Lankford coefficients are plotted against the tensile direction in Fig. 7. The Lankford coefficient (strain ratio) is defined as

$$R_\alpha = \frac{d\varepsilon_\perp}{d\varepsilon_{\mathrm{ND}}} \tag{10}$$

where $d\varepsilon_\perp$ is the incremental strain in the direction perpendicular to the tensile direction α lying in the ED–TD plane and $d\varepsilon_{\mathrm{ND}}$ is the incremental strain in the thickness direction (ND). Thus, the Lankford coefficient R_α gives the evolution of the cross section of the specimen. Similarly to the normalized yield stress, the values and variation in the Lankford coefficient with tensile direction are distinct for the two alloys due to their different textures. Even if there are differences between the experimental and numerical values of the Lankford coefficients, the results show the strong influence of the crystallographic texture on the plastic flow. The predicted values of the Lankford coefficients in the 45° and 90° directions for the AA6110 alloy deviate from the experimental values, but are similar to values typically observed experimentally for aluminium alloys with a non-recrystallized microstructure (see, e.g., Fourmeau et al., 2011).

As observed in Fig. 4, the failure strain varies with the tensile direction, and Fig. 8 presents the failure strain versus tensile direction for the two alloys. It is apparent that the failure strain varies significantly for these anisotropic alloys. The failure strain from the experimental tests of the AA6063 alloy, and thus its tensile ductility, is the greatest in the 90° direction and the lowest in the 45° direction. For the AA6110 alloy it is the opposite, where the failure strain is the greatest in the 45° direction and the lowest in the 90° direction. These observations conform well with experimental results in the literature for aluminium alloys with similar grain structures and crystallographic textures (Fourmeau et al., 2013; Khadyko et al., 2019). It is further found that the finite element analyses are able to capture the main variation of the failure strain with tensile direction for both alloys, which highlights the marked influence of the plastic anisotropy, and thus of the crystallographic texture and its evolution, on the anisotropic failure of these alloys. Comparing the variation of the failure strain in Fig. 8 with the variation of the Lankford coefficient in Fig. 7, it is found that these two characteristics exhibit to some extent the same trends,

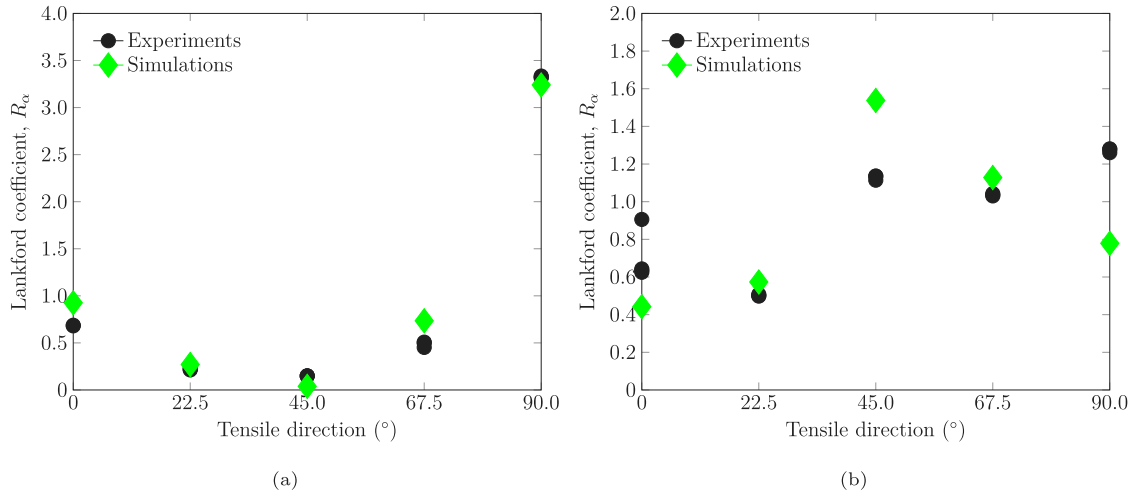

Fig. 7. Lankford coefficient versus tensile direction for the (a) AA6063 alloy and (b) AA6110 alloy up to necking.

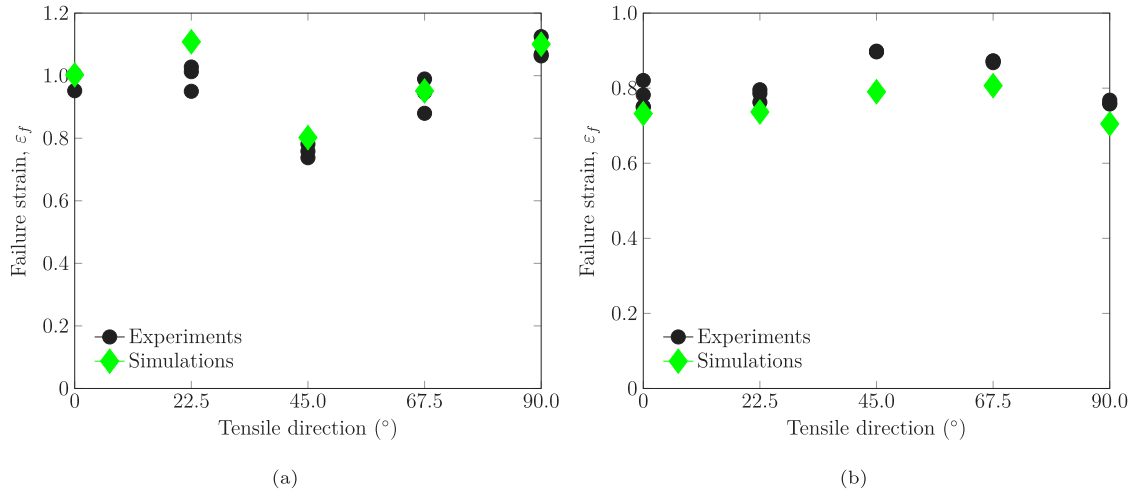

Fig. 8. Failure strain versus tensile direction for the (a) AA6063 alloy and (b) AA6110 alloy.

i.e., the two quantities appear to exhibit a minimum and maximum at the same tensile directions.

The fracture surfaces from the crystal plasticity finite element analyses and the experimental tests are presented in Figs. 9 and 10 for the AA6063 and AA6110 alloys, respectively. The fracture surface is defined as the surface created by element erosion in the finite element analyses. Due to the strong crystallographic texture of the two alloys, different shapes of the fracture surfaces are observed in different tensile directions and between the two alloys. The shape of the fracture surface changes from circular to elliptical with the long axis either being horizontal or vertical, depending on the Lankford coefficient at a given tensile direction. Comparing the fracture surface shapes from the finite element simulations and experimental tests, we observe an overall agreement, but there are some discrepancies in tensile directions where the predicted Lankford coefficient deviates significantly from the experimental one. These deviations are likely related to the dependence of the plastic anisotropy on the heat treatment observed by Khadyko et al. (2017) for the AA6063 alloy, a dependence that the single crystal plasticity model used in this study is unable to describe. Contours of the von Mises equivalent plastic strain are depicted on the surface of the simulated specimen in different tensile directions in the figures. To this end, the von Mises equivalent plastic strain is defined as

$$\varepsilon^p_{eq} = \int_0^t \sqrt{\frac{2}{3} D^p_{ij} D^p_{ij}}\, dt \tag{11}$$

where $\mathbf{D}^p$ is the plastic part of the rate of deformation tensor. Due to differences in the crystallographic orientation between grains, the local deformation is heterogeneous, creating shear bands which can be observed as contours on the exterior of the specimen next to the fracture surface. As individual grains with distinct orientations will rotate and deform differently, a roughness, i.e., orange peel, develops on the surface of the specimens both in the finite element analyses and experimental tests. Considering the fracture surfaces from the numerical analyses more closely, it is clear that they are not entirely flat, but resemble the cup-and-cone or cup-and-cup fracture surfaces with grooves and indents observed from the experimental fracture surfaces of the two alloys.

The diameters of the fracture surfaces of the smooth axisymmetric tensile specimen in different tensile directions are presented in Table 3 for the experimental tests and the finite element analyses depicted in Figs. 9 and 10. The diameters are along the thickness direction, D_{ND}, and the direction perpendicular to the tensile direction and the thickness direction lying in the ED–TD plane, $D_{\perp}$. While the simulations capture the general trends seen in the experiments, indicating the strong influence of the crystallographic texture, there are important deviations that could be caused by other sources of anisotropy, such as the grain morphology, and the coarse representation of the microstructure in the finite element models. In Table 4 the corresponding fracture strains calculated based on the diameters of the fracture surfaces are

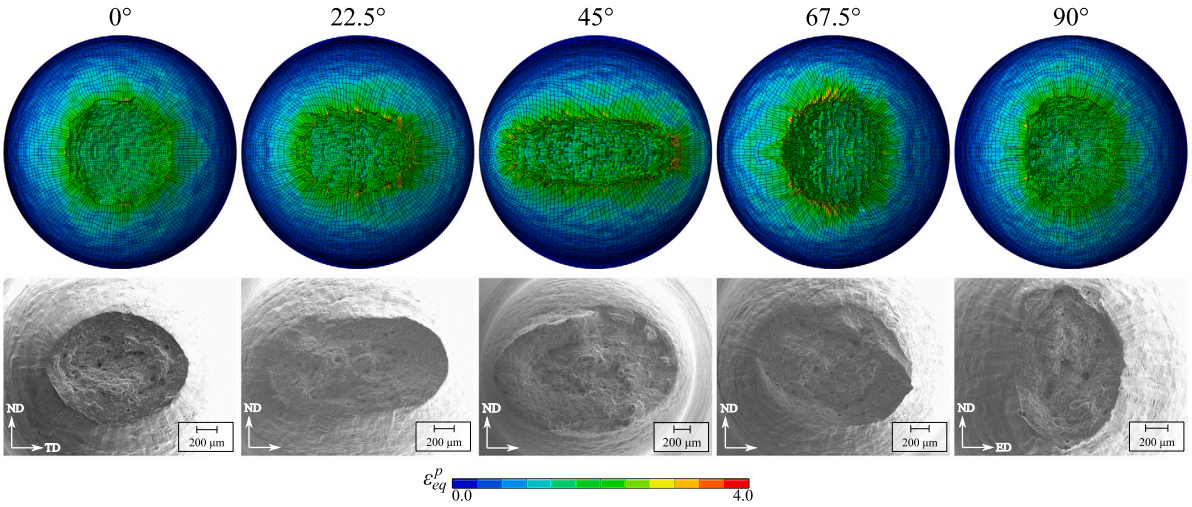

Fig. 9. Fracture surfaces in different tensile directions for the AA6063 alloy from finite element analyses (top) and experiments (bottom). Contours of the von Mises equivalent plastic strain are shown on the deformed meshes.

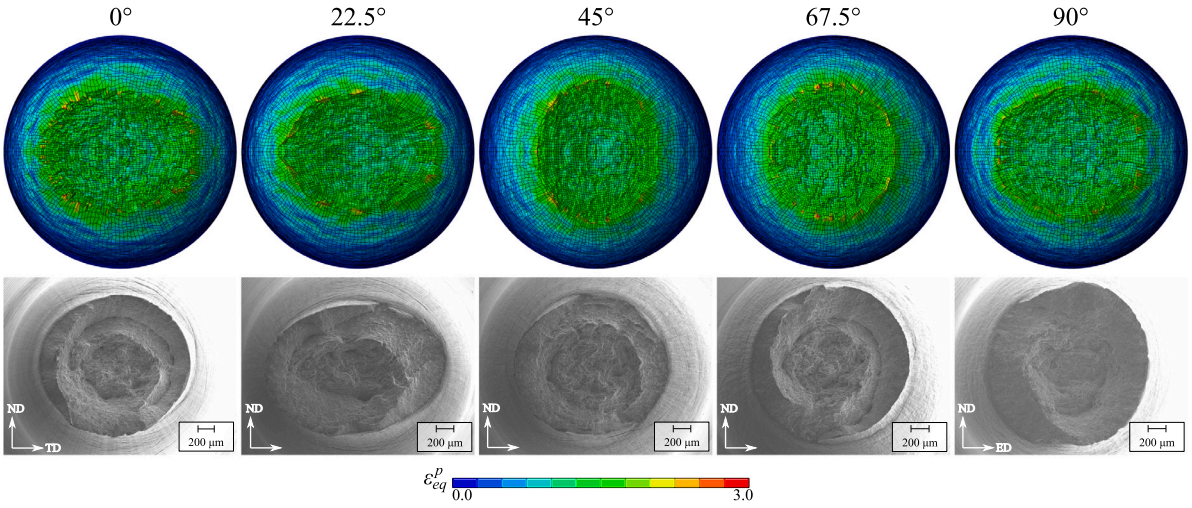

Fig. 10. Fracture surfaces in different tensile directions for the AA6110 alloy from finite element analyses (top) and experiments (bottom). Contours of the von Mises equivalent plastic strain are shown on the deformed meshes.

Table 3
Predicted versus experimental diameters of the fracture surfaces along two perpendicular directions for the tensile specimens. The diameter $D_{\perp}$ is along the direction perpendicular to the loading direction lying in the ED–TD plane and D_{ND} is along ND.

Material	0°		22.5°		45°		67.5°		90°	
	$D_{\perp}$ (mm)	D_{ND} (mm)	$D_{\perp}$ (mm)	D_{ND} (mm)	$D_{\perp}$ (mm)	D_{ND} (mm)	$D_{\perp}$ (mm)	D_{ND} (mm)	$D_{\perp}$ (mm)	D_{ND} (mm)
AA6063										
Experimental	1.41	1.12	1.79	0.97	2.24	1.42	1.70	1.32	1.01	1.49
Simulations	1.32	1.30	1.61	1.06	2.18	1.02	1.41	1.36	1.14	1.46
AA6110										
Experimental	1.85	1.75	2.06	1.47	1.76	1.57	1.75	1.67	1.83	1.82
Simulations	1.93	1.52	1.96	1.62	1.49	1.82	1.66	1.68	1.77	1.66

given together with the average failure strains in different tensile directions. The fracture strain is markedly larger than the failure strain but exhibits the same overall trend in the variation with tensile direction.

Fig. 11 presents a longitudinal section in the ED–TD plane through the centre of the tensile specimen in different tensile directions from the finite element analyses of the two alloys. On the exterior surface of the deformed specimens, the orange peel can be observed, and the heterogeneous strain field is clearly seen in the sectional view for each tensile direction. Signs of shear bands can also be seen close to the fracture surfaces for both alloys. These shear bands form early in the deformation process and persist until fracture. This is readily seen in Fig. 12 where the centre of the specimen in the 45° direction for both alloys is depicted throughout the deformation process. With straining, the deformation is observed to localize in the centre of the specimen and a slant plastic strain band forms for the AA6063 alloy in the 45° direction, whereas the deformation and localization of plastic deformation are more symmetric for the AA6110 alloy. After failure, elements start to erode from the centre of the specimen where the stress triaxiality and the damage variable are the greatest. The crack formed by element erosion then propagates towards the edge of the

Table 4
Predicted versus average experimental failure strain ε_f and fracture strain ε_F in different tensile directions. The fracture strains are calculated based on the diameters of the fracture surfaces measured post-mortem and given in Table 3, while the failure strains are given as the logarithmic strain at failure corresponding to the point of maximum true stress.

Material	0°		22.5°		45°		67.5°		90°	
	ε_f	ε_F	ε_f	ε_F	ε_f	ε_F	ε_f	ε_F	ε_f	ε_F
AA6063										
Experimental	0.98	1.74	1.00	1.64	0.76	1.04	0.94	1.39	1.09	1.79
Simulations	1.00	1.66	1.11	1.66	0.80	1.40	0.95	1.55	1.10	1.69
AA6110										
Experimental	0.78	1.02	0.78	1.09	0.90	1.18	0.87	1.12	0.76	0.99
Simulations	0.73	1.12	0.74	1.04	0.79	1.20	0.81	1.17	0.71	1.12

specimen and the stress level drops rapidly and steadily until final separation of the specimen. This rapid and steady drop in the true stress level is also observed experimentally for the investigated alloys, see Thomesen et al. (2021). Looking at the fractured specimens in Fig. 11, the AA6063 alloy displays a cup-and-cup type of fracture surface in the 0° and 90° directions, while a more slant or asymmetric fracture mode is found in the other in-plane directions. In contrast, the AA6110 alloy exhibits a cup-and-cone or a cup-and-cup type of fracture surface in all the tensile directions. Again, due to the heterogeneous plastic flow caused by the discrete nature of individual grains with different crystallographic orientations, the fracture surfaces are heterogeneous and quite irregular. These fracture modes are largely consistent with the experimental results where a symmetric cup-and-cup type of fracture surface is observed for the AA6063 alloy in the 0° and 90° directions, and a slant fracture surface is found in the 22.5°, 45° and 67.5° directions. The fracture surfaces predicted for the AA6110 alloy agree well with the experiments, where a cup-and-cone fracture surface is found in all the tensile directions.

5. Discussion

A variation in the failure and fracture strain with tensile direction, i.e., fracture anisotropy, is observed for the two aluminium alloys investigated in this study, see Figs. 4 and 8 and Table 4. The fracture anisotropy appears to be closely linked to the plastic anisotropy of the alloys, which is supported by the overall agreement between the experiments and the crystal plasticity finite element simulations where crystallographic texture is the only source of anisotropy. These results agree with previous experimental and numerical results on 6000- and 7000-series aluminium alloys (Fourmeau et al., 2013; Morin et al., 2018; Khadyko et al., 2019; Frodal et al., 2020a). Frodal et al. (2020a) found that the failure strain predicted by strain localization analyses showed similar trends to the variation of the Lankford coefficient with tensile direction for three anisotropic 6000-series aluminium alloys. The crystal plasticity finite element analyses performed in this study are able to describe and predict the fracture anisotropy of the experimental tests with good accuracy by accounting for the crystallographic textures of the alloys. The damage and failure model used in this study, see Eq. (7), is independent of any direction, and damage evolution is governed by the stress triaxiality ratio and the accumulated plastic shear strain rate. It follows that the predicted fracture anisotropy in these analyses stems solely from the anisotropy in yielding and plastic flow introduced by the crystallographic texture. It is thus a reasonable conjecture that the fracture anisotropy of the two textured aluminium alloys investigated is primarily an effect of the crystallographic texture also in the experimental tests.

Albeit plastic anisotropy is likely the major contributor to fracture anisotropy of the alloys investigated herein, other sources of anisotropy can influence the ductile fracture process and affect the fracture anisotropy. Even materials exhibiting nearly isotropic yielding and plastic flow can exhibit fracture anisotropy because of morphological or topological anisotropy caused by the shape, orientation and spatial distribution of voids and particles (Hannard et al., 2018; Marteleur et al., 2021). The damage process through nucleation, growth and coalescence of voids may also introduce anisotropy effects (Madi et al., 2019) by, e.g., favouring particle cracking in certain material directions (Agarwal et al., 2002).

The ductile fracture process occurs inside grains or at the grain boundaries, and the grains could for some materials be one or two orders of magnitude larger than the void-nucleating particles. For the alloys investigated in this study, the equivalent diameter of the constituent particles is on average 1 μm and the size of the grains is some tens of micrometres, see Section 2. Thus, in a single grain there will be some hundred constituent particles for the alloys investigated. Consequently, void growth around a particle takes place in a single grain/crystal or possibly within some few grains when the void grows on or in the neighbourhood of the grain boundary. Therefore, it is advantageous to model the matrix behaviour using crystal plasticity as to include the strongly anisotropic behaviour of single crystals in the damage process. As a result, heterogeneous stress and deformation fields develop in these materials that are essential for a realistic description of ductile fracture as they promote strain localization, damage evolution and ultimately crack initiation. Due to the fact that the individual grains are oriented differently with respect to the tensile axis in the tensile tests in different directions, the plastic deformation, shear band formation and strain localization are unique for each direction. The influence of this inherent heterogeneity of the alloy is lost in conventional analyses using constitutive models where the plasticity and damage processes have been homogenized.

In this study, an equi-axed grain structure is used in the finite element analyses for the two alloys. The fibrous grain structure of the AA6110 alloy is not accounted for in the microstructural modelling of the material. Owing to the computational complexity of modelling a fibrous grain structure with extremely thin elongated grains, it is currently not feasible to model such grain structures in three-dimensional engineering specimens or small structural components with the crystal plasticity finite element method, albeit available in representative volume element (RVE) simulations. It has previously been shown that the grain structure of an alloy can have an influence on the plastic anisotropy of the material using RVE calculations (Delannay et al., 2009). A higher resolution mesh with a finer discretization, i.e., several elements per grain, could have resolved the inter-grain gradients and given a more accurate description of the underlying microstructure, but at the cost of significantly increasing the computational time. The finite element analyses with a one-element-per-grain representation are deemed sufficient in this study as they are able to accurately describe the initial plastic anisotropy, the evolution of the plastic anisotropy by texture evolution, the fracture mode and the fracture anisotropy. The damage variable represents, in an average sense, the nonuniform damage process in a single grain. Recently, nonuniform slip resistances and crystal orientations within each grain have been found to influence the plastic anisotropy (Park et al., 2021). As such, the grain structure and the non-uniformity inside of grains will also most likely have an effect on the fracture anisotropy of a given material.

Precipitate strengthened aluminium alloys have precipitate free zones (PFZs) along grain boundaries. The width of these zones is typically from a few tens to some hundreds of nanometres (Frodal et al., 2020b). Due to their tiny scale, the PFZs are impossible to explicitly include in modelling of engineering specimens with the computational resources available today. Since the PFZs lack strengthening precipitates, they are softer than the rest of the grain and may promote strain localization and ductile fracture (Dowling and Martin, 1976; Morgeneyer et al., 2008; Khadyko et al., 2016). Owing to this localization of deformation, the PFZs may develop significant misorientations relative to their parent grains, which in turn could contribute to the

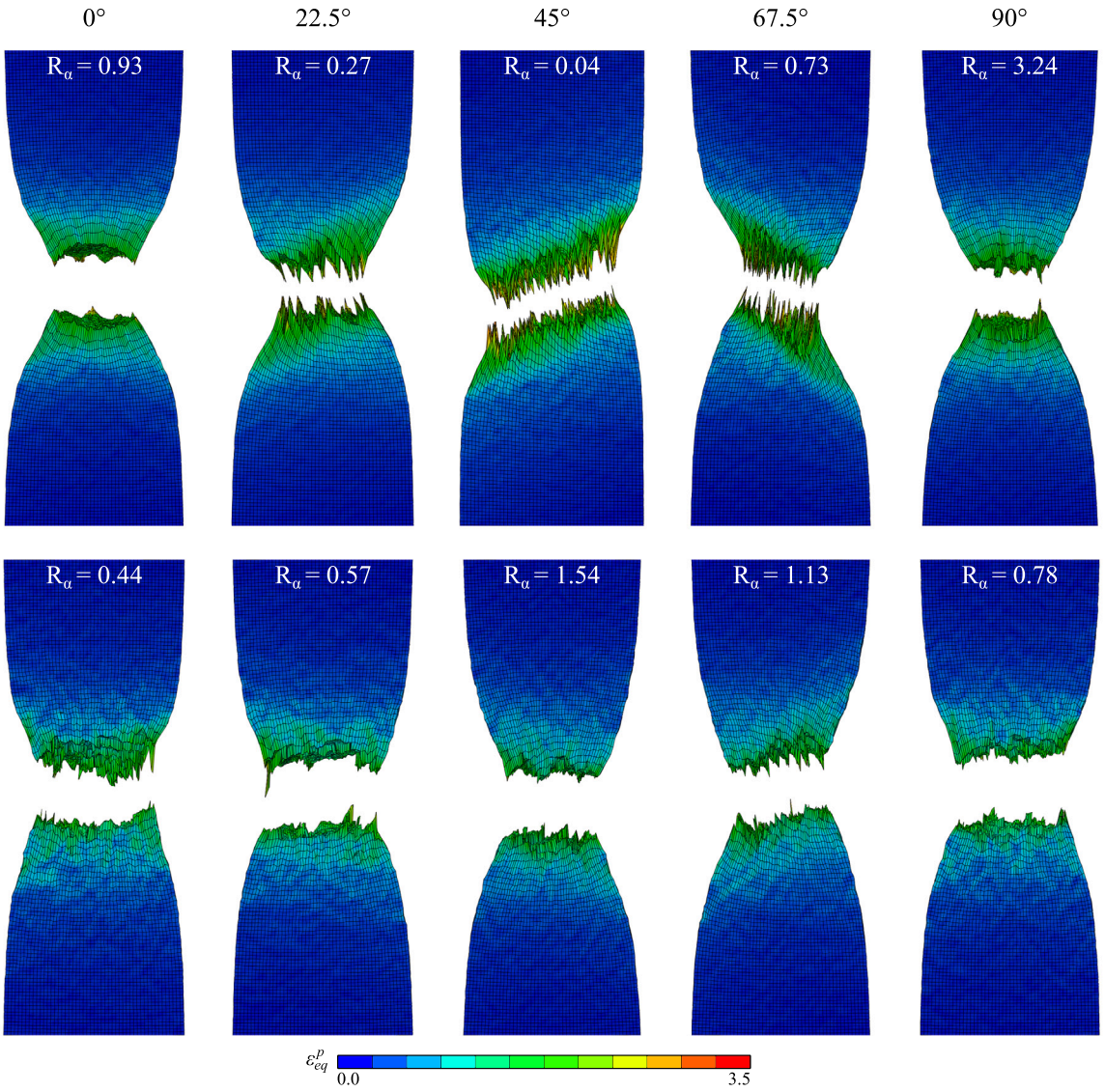

Fig. 11. Longitudinal section through the centre of the fractured tensile specimens in different tensile directions from the finite element analyses depicted in the ED–TD plane for: the AA6063 alloy (top), and the AA6110 alloy (bottom). The Lankford coefficient R_α of the corresponding test is depicted on the top of each finite element mesh. Contours of the von Mises equivalent plastic strain are shown on the deformed meshes.

strengthening of the PFZs (Christiansen et al., 2018) and thus also delay fracture initiation. Because of their influence on ductile fracture, the PFZs may also have an effect on the fracture anisotropy in textured aluminium alloys (Steglich et al., 2008). The PFZs' role and effect in the ductile fracture process is still an open question and further research on this topic is needed.

The ductile fracture process, consisting of nucleation, growth and coalescence of microscopic voids at constituent particles or inclusions, depends on the local stress state and the microstructure of the material in a complex way. Several microstructural features may influence the fracture strain of a material by promoting or postponing damage evolution. Two of the most important material characteristics controlling ductile fracture and the magnitude of the fracture strain are the size and volume fraction of constituent particles (Benzerga and Leblond, 2010; Pineau et al., 2016; Hannard et al., 2016, 2017; Tomstad et al., 2021). In contrast, the size and volume fraction of particles probably have little influence on the fracture anisotropy. However, for two alloys with similar precipitate structure, grain structure and initial texture, a difference in fracture anisotropy between the alloys might appear if one alloy has a sufficiently high failure strain as to allow for substantial texture evolution, while the other alloy does not.

6. Concluding remarks

The origin of the fracture anisotropy encountered in textured aluminium alloys was investigated by conducting finite element simulations on axisymmetric smooth tensile specimens. The numerical results were compared to existing experimental data from tensile tests in five different in-plane material directions. The two extruded alloys considered, i.e., AA6063 and AA6110, had different yield strength, work hardening, grain structure, crystallographic texture, and tensile ductility. The coupled damage and single crystal plasticity model of Frodal et al. (2021) allowed for finite element analyses of engineering test specimens where each grain was explicitly modelled. This approach allowed for the local heterogeneous stress and strain fields caused by the microstructure and their influence on ductile fracture to be investigated. In the numerical simulations, tendencies of shear bands were observed, which may lead to strain localization and ductile fracture.

The main conclusions of the study are summarized as follows:

- Owing to the distinct crystallographic texture of the extruded alloys, their plastic anisotropy is significant. The differences in

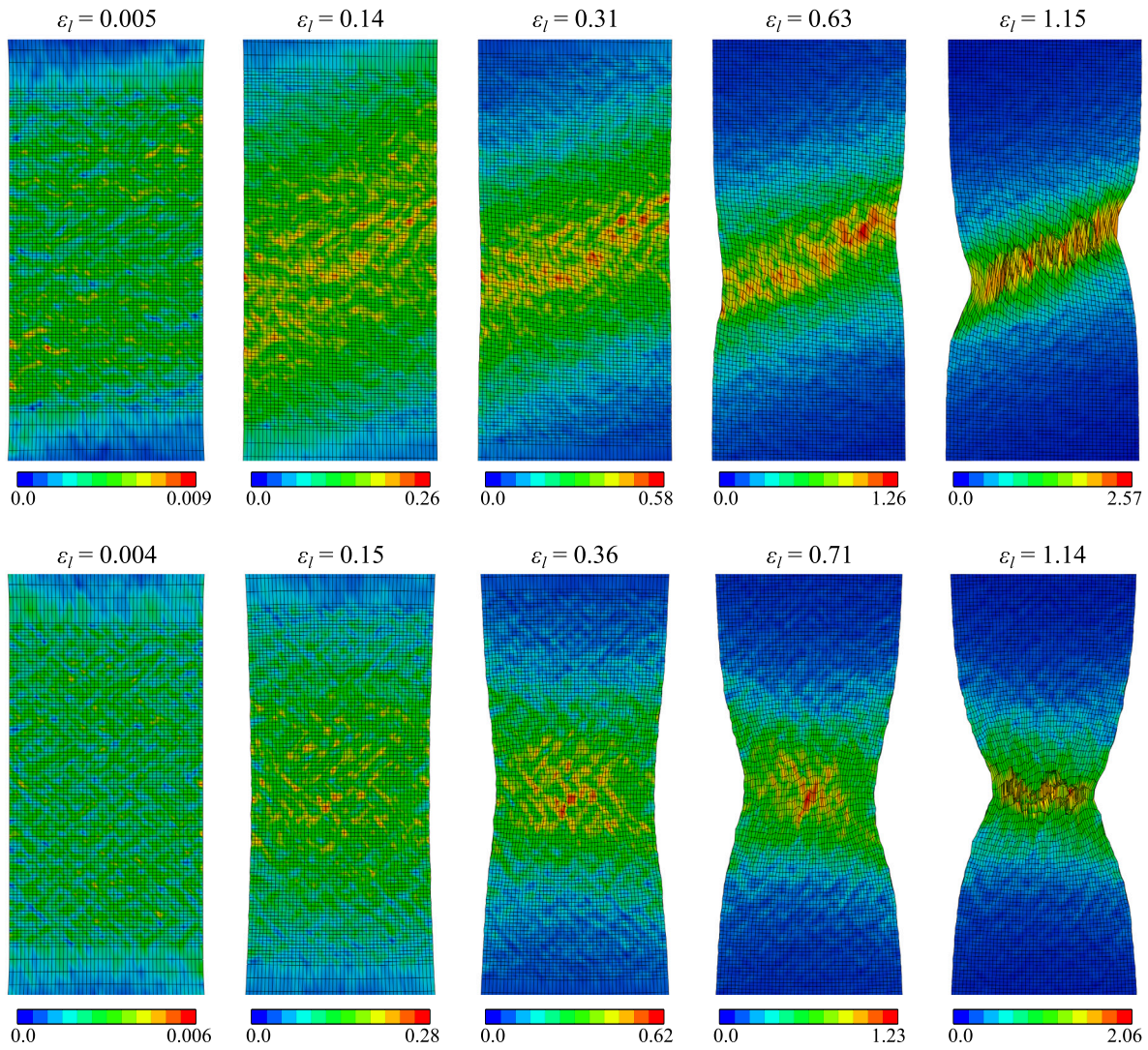

Fig. 12. Deformed configuration plots from the centre of the tensile specimens in the 45° direction at different stages during the deformation process from the finite element analyses depicted in the ED–TD plane for: the AA6063 alloy (top), and the AA6110 alloy (bottom). Contours of the von Mises equivalent plastic strain are shown on the deformed meshes and the corresponding logarithmic strain ε_l is depicted above each mesh.

yielding and plastic flow result in different shapes of the fracture surfaces in different tensile directions and between the alloys.

- Anisotropy in the yielding, work hardening and plastic flow is captured with the crystal plasticity framework by accounting for the crystallographic texture and the texture evolution.
- The overall agreement between the experimental and numerical fracture surface shapes highlights the marked influence of the crystallographic texture on the plastic flow.
- As the damage evolution in different grains is affected by their crystallographic orientation and the local stress and strain fields, the fracture surfaces from the crystal plasticity simulations exhibit features such as grooves and indents observable also on the experimental fracture surfaces.
- The crystal plasticity finite element simulations capture both the plastic anisotropy and the fracture anisotropy of the textured aluminium alloys using a scalar damage model, which indicates that the primary source of fracture anisotropy for these materials is the crystallographic texture.

The crystal plasticity finite element framework adopted in this study will be further used in detailed simulations to study the effects of material heterogeneity, grain structure, and crystallographic texture on the shear band formation and ductility of materials subjected to different loading scenarios.

Declaration of competing interest

The authors declare that they have no known competing financial interests or personal relationships that could have appeared to influence the work reported in this paper.

Acknowledgements

The authors gratefully appreciate the financial support from the Norwegian University of Science and Technology (NTNU), Norway and the Research Council of Norway through the FRINATEK Program FractAl, Project No. 250553, and from the Centre for Advanced Structural Analysis (CASA), Norway, Project No. 237885.

References

Agarwal, H., Gokhale, A.M., Graham, S., Horstemeyer, M.F., 2002. Anisotropy of intermetallic particle cracking damage evolution in an Al-Mg-Si base wrought aluminum alloy under uniaxial compression. Metall. Mater. Trans. A 33 (11), 3443–3448.

Bachmann, F., Hielscher, R., Schaeben, H., 2010. Texture analysis with MTEX – Free and open source software toolbox. Solid State Phenom. 160, 63–68.
Barlat, F., Aretz, H., Yoon, J.W., Karabin, M.E., Brem, J.C., Dick, R.E., 2005. Linear transfomation-based anisotropic yield functions. Int. J. Plast. 21 (5), 1009–1039.
Benzerga, A.A., Leblond, J.-B., 2010. Ductile fracture by void growth to coalescence. Adv. Appl. Mech. 44, 169–305.
Benzerga, A.A., Thomas, N., Herrington, J.S., 2019. Plastic flow anisotropy drives shear fracture. Sci. Rep. 9 (1), 1425.
Bron, F., Besson, J., 2004. A yield function for anisotropic materials Application to aluminum alloys. Int. J. Plast. 20 (4), 937–963.
Campbell, J., 2011. The origin of griffith cracks. Metall. Mater. Trans. B 42 (6), 1091–1097.
Chen, J., Madi, Y., Morgeneyer, T.F., Besson, J., 2011. Plastic flow and ductile rupture of a 2198 Al–Cu–Li aluminum alloy. Comput. Mater. Sci. 50 (4), 1365–1371.
Christiansen, E., Marioara, C.D., Marthinsen, K., Hopperstad, O.S., Holmestad, R., 2018. Lattice rotations in precipitate free zones in an Al-Mg-Si alloy. Mater. Charact. 144, 522–531.
Delannay, L., Melchior, M.A., Signorelli, J.W., Remacle, J.F., Kuwabara, T., 2009. Influence of grain shape on the planar anisotropy of rolled steel sheets – evaluation of three models. Comput. Mater. Sci. 45 (3), 739–743.
Dowling, J.M., Martin, J.W., 1976. The influence of MN additions on the deformation behaviour of an Al-Mg-Si alloy. Acta Metall. 24 (12), 1147–1153.
Engler, O., Randle, V., 2009. Introduction to Texture Analysis: Macrotexture, Microtexture, and Orientation Mapping, second ed. CRC press, Taylor & Francis Group.
Feather, W.G., Ghorbanpour, S., Savage, D.J., Ardeljan, M., Jahedi, M., McWilliams, B.A., Gupta, N., Xiang, C., Vogel, S.C., Knezevic, M., 2019. Mechanical response, twinning, and texture evolution of WE43 magnesium-rare earth alloy as a function of strain rate: Experiments and multi-level crystal plasticity modeling. Int. J. Plast. 120, 180–204.
Fourmeau, M., Børvik, T., Benallal, A., Hopperstad, O.S., 2013. Anisotropic failure modes of high-strength aluminium alloy under various stress states. Int. J. Plast. 48, 34–53.
Fourmeau, M., Børvik, T., Benallal, A., Lademo, O.G., Hopperstad, O.S., 2011. On the plastic anisotropy of an aluminium alloy and its influence on constrained multiaxial flow. Int. J. Plast. 27 (12), 2005–2025.
Frodal, B.H., Christiansen, E., Myhr, O.R., Hopperstad, O.S., 2020b. The role of quench rate on the plastic flow and fracture of three aluminium alloys with different grain structure and texture. Internat. J. Engrg. Sci. 150, 103257.
Frodal, B.H., Dæhli, L.E.B., Børvik, T., Hopperstad, O.S., 2019. Modelling and simulation of ductile failure in textured aluminium alloys subjected to compression-tension loading. Int. J. Plast. 118, 36–69.
Frodal, B.H., Morin, D., Børvik, T., Hopperstad, O.S., 2020a. On the effect of plastic anisotropy, strength and work hardening on the tensile ductility of aluminium alloys. Int. J. Solids Struct. 188–189, 118–132.
Frodal, B.H., Pedersen, K.O., Børvik, T., Hopperstad, O.S., 2017. Influence of pre-compression on the ductility of AA6xxx aluminium alloys. Int. J. Fract. 206 (2), 131–149.
Frodal, B.H., Thomesen, S., Børvik, T., Hopperstad, O.S., 2021. On the coupling of damage and single crystal plasticity for ductile polycrystalline materials. Int. J. Plast. 142, 102996.
Ghorbanpour, S., Alam, M.E., Ferreri, N.C., Kumar, A., McWilliams, B.A., Vogel, S.C., Bicknell, J., Beyerlein, I.J., Knezevic, M., 2020. Experimental characterization and crystal plasticity modeling of anisotropy, tension-compression asymmetry, and texture evolution of additively manufactured Inconel 718at room and elevated temperatures. Int. J. Plast. 125, 63–79.
Gurson, A.L., 1977. Continuum theory of ductile rupture by void nucleation and growth: Part I—Yield criteria and flow rules for porous ductile media. J. Eng. Mater. Technol. 99, 2–15.
Hannard, F., Castin, S., Maire, E., Mokso, R., Pardoen, T., Simar, A., 2017. Ductilization of aluminium alloy 6056 by friction stir processing. Acta Mater. 130, 121–136.
Hannard, F., Pardoen, T., Maire, E., Le Bourlot, C., Mokso, R., Simar, A., 2016. Characterization and micromechanical modelling of microstructural heterogeneity effects on ductile fracture of 6xxx aluminium alloys. Acta Mater. 103, 558–572.
Hannard, F., Simar, A., Maire, E., Pardoen, T., 2018. Quantitative assessment of the impact of second phase particle arrangement on damage and fracture anisotropy. Acta Mater. 148, 456–466.
Hill, R., 1948. A theory of the yielding and plastic flow of anisotropic metals. Proc. R. Soc. A 193 (1033), 281–297.
Jia, N., Roters, F., Eisenlohr, P., Kords, C., Raabe, D., 2012. Non-crystallographic shear banding in crystal plasticity FEM simulations: Example of texture evolution in α-brass. Acta Mater. 60 (3), 1099–1115.
Kalidindi, S.R., Donohue, B.R., Li, S., 2009. Modeling texture evolution in equal channel angular extrusion using crystal plasticity finite element models. Int. J. Plast. 25 (5), 768–779.
Keralavarma, S.M., Hoelscher, S., Benzerga, A.A., 2011. Void growth and coalescence in anisotropic plastic solids. Int. J. Solids Struct. 48 (11), 1696–1710.
Khadyko, M., Marioara, C.D., Dumoulin, S., Børvik, T., Hopperstad, O.S., 2017. Effects of heat-treatment on the plastic anisotropy of extruded aluminium alloy AA6063. Mater. Sci. Eng. A 708, 208–221.
Khadyko, M., Marioara, C.D., Ringdalen, I.G., Dumoulin, S., Hopperstad, O.S., 2016. Deformation and strain localization in polycrystals with plastically heterogeneous grains. Int. J. Plast. 86, 128–150.
Khadyko, M., Morin, D., Børvik, T., Hopperstad, O.S., 2019. Tensile ductility of extruded aluminium alloy AA6063 in different tempers. Mater. Sci. Eng. A 744, 500–511.
Legarth, B.N., Tvergaard, V., 2018. Effects of plastic anisotropy and void shape on full three-dimensional void growth. J. Appl. Mech. 85 (5), 051007.
Lemaitre, J., 1985. A continuous damage mechanics model for ductile fracture. J. Eng. Mater. Technol. 107 (1), 83–89.
Li, S., Kalidindi, S.R., Beyerlein, I.J., 2005. A crystal plasticity finite element analysis of texture evolution in equal channel angular extrusion. Mater. Sci. Eng. A 410–411, 207–212.
Lu, C., Deng, G.Y., Tieu, A.K., Su, L.H., Zhu, H.T., Liu, X.H., 2011. Crystal plasticity modeling of texture evolution and heterogeneity in equal channel angular pressing of aluminum single crystal. Acta Mater. 59 (9), 3581–3592.
Madi, Y., Garcia, J.M., Proudhon, H., Shinohara, Y., Helfen, L., Besson, J., Morgeneyer, T.F., 2019. On the origin of the anisotropic damage of X100 line pipe steel: Part I—In situ synchrotron tomography experiments. Integr. Mater. Manuf. Innov. 8, 570–596.
Maire, E., Zhou, S., Adrien, J., Dimichiel, M., 2011. Damage quantification in aluminium alloys using in situ tensile tests in X-ray tomography. Eng. Fract. Mech. 78 (15), 2679–2690.
Marteleur, M., Leclerc, J., Colla, M.-S., Nguyen, V.-D., Noels, L., Pardoen, T., 2021. Ductile fracture of high strength steels with morphological anisotropy, Part I: Characterization, testing, and void nucleation law. Eng. Fract. Mech. 244, 107569.
Morgeneyer, T.F., Khadyko, M., Buljac, A., Helfen, L., Hild, F., Benallal, A., Børvik, T., Hopperstad, O.S., 2021. On crystallographic aspects of heterogeneous plastic flow during ductile tearing: 3D measurements and crystal plasticity simulations for AA7075-T651. Int. J. Plast. 144, 103028.
Morgeneyer, T.F., Starink, M.J., Wang, S.C., Sinclair, I., 2008. Quench sensitivity of toughness in an Al alloy: Direct observation and analysis of failure initiation at the precipitate-free zone. Acta Mater. 56 (12), 2872–2884.
Morin, D., Fourmeau, M., Børvik, T., Benallal, A., Hopperstad, O.S., 2018. Anisotropic tensile failure of metals by the strain localization theory: An application to a high-strength aluminium alloy. Eur. J. Mech. A Solids 69, 99–112.
Park, T., Lim, H., Reedlunn, B., Kramer, S., Corona, E., Pourboghrat, F., 2021. The impact of heterogeneous microstructural features on crystal plasticity modeling of plastic anisotropy. Modelling Simulation Mater. Sci. Eng. 29 (7), 075004.
Pineau, A., Benzerga, A., Pardoen, T., 2016. Failure of metals I: Brittle and ductile fracture. Acta Mater. 107, 424–483.
Prakash, A., Weygand, S.M., Riedel, H., 2009. Modeling the evolution of texture and grain shape in Mg alloy AZ31 using the crystal plasticity finite element method. Comput. Mater. Sci. 45 (3), 744–750.
Rice, J.R., Tracey, D.M., 1969. On the ductile enlargement of voids in triaxial stress fields. J. Mech. Phys. Solids 17 (3), 201–217.
Rousselier, G., 1987. Ductile fracture models and their potential in local approach of fracture. Nucl. Eng. Des. 105 (1), 97–111.
Scherer, J.-M., Besson, J., Forest, S., Hure, J., Tanguy, B., 2021. A strain gradient plasticity model of porous single crystal ductile fracture. J. Mech. Phys. Solids 156, 104606.
Steglich, D., Brocks, W., Heerens, J., Pardoen, T., 2008. Anisotropic ductile fracture of Al 2024 alloys. Eng. Fract. Mech. 75 (12), 3692–3706.
Thomesen, S., 2019. Plastic Flow and Fracture of Isotropic and Anisotropic 6000-Series Aluminium Alloys: Experiments and Numerical Simulations (Ph.D. thesis). NTNU.
Thomesen, S., Hopperstad, O.S., Børvik, T., 2021. Anisotropic plasticity and fracture of three 6000-series aluminum alloys. Metals 11 (4).
Toda, H., Oogo, H., Horikawa, K., Uesugi, K., Takeuchi, A., Suzuki, Y., Nakazawa, M., Aoki, Y., Kobayashi, M., 2013. The true origin of ductile fracture in aluminum alloys. Metall. Mater. Trans. A 45 (2), 765–776.
Tomstad, A.J., Thomesen, S., Børvik, T., Hopperstad, O.S., 2021. Effects of constituent particle content on ductile fracture in isotropic and anisotropic 6000-series aluminium alloys. Mater. Sci. Eng. A 820, 141420.
Torki, M.E., Benzerga, A.A., 2018. A mechanism of failure in shear bands. Extreme Mech. Lett. 23, 67–71.
Tvergaard, V., 1981. Influence of voids on shear band instabilities under plane strain conditions. Int. J. Fract. 17 (4), 389–407.
Wu, X., Kalidindi, S.R., Necker, C., Salem, A.A., 2007. Prediction of crystallographic texture evolution and anisotropic stress–strain curves during large plastic strains in high purity α-titanium using a taylor-type crystal plasticity model. Acta Mater. 55 (2), 423–432.
Zhang, H., Diehl, M., Roters, F., Raabe, D., 2016. A virtual laboratory using high resolution crystal plasticity simulations to determine the initial yield surface for sheet metal forming operations. Int. J. Plast. 80, 111–138.
Zhang, K., Holmedal, B., Hopperstad, O.S., Dumoulin, S., Gawad, J., Van Bael, A., Van Houtte, P., 2015. Multi-level modelling of mechanical anisotropy of commercial pure aluminium plate: Crystal plasticity models, advanced yield functions and parameter identification. Int. J. Plast. 66, 3–30.